Gust-aerofoil coupling with a loaded aerofoil*

Anna M. Young†
University of Bath, Claverton Down Road, BA2 7AY, UK.

Amanda S. M. Smyth‡
University of Cambridge, Cambridge, CB3 0DY, UK

The unsteady load response of an aerofoil encountering a gust is often modelled using analytical transfer functions, which assume idealised behaviour of both the flow and the aerofoil. One such transfer function is the Sears function, which models a pure transverse gust interacting with a flat-plate aerofoil at zero mean incidence. The function was extended by Goldstein and Atassi to account for camber and incidence as well as the presence of a streamwise gust component. Atassi showed that the effects of camber and incidence (i.e. non-zero mean aerofoil loading) are not negligible when there is a streamwise gust component. In this work, new experimental data is shown for an aerofoil with non-zero loading encountering a gust with both streamwise and transverse components. As well as giving validation to the Atassi model, the flow physics behind the model is shown, including the superposition of the gust onto the aerofoil potential field and the propagation of the gust along the aerofoil surface.

Nomenclature

A_N, B_N	=	Fourier Coefficients
c	=	Aerofoil chord
$C_P = \frac{P-P_{in}}{P_{0in}-P_{in}}$	=	Pressure coefficient
$C_L = \frac{L}{\frac{1}{2}\rho U_\infty}$	=	Lift coefficient
f	=	Frequency (Hz)
$k_1 = 2\pi\frac{f\,c}{U_\infty}$	=	Reduced frequency of transverse gust
k_2	=	Reduced frequency of streamwise gust
L	=	Lift (N)
m	=	Aerofoil camber (% chord)
P	=	Pressure
R	=	Unsteady lift normalised by quasi-steady lift

*An earlier version of this paper was published at the AIAA SciTech as Paper AIAA 2020-0558
†Lecturer, Department of Mechanical Engineering
‡Research Associate, Whittle Laboratory

S = Sears function

t = Time

u = Streamwise velocity perturbation (m/s)

v = Transverse velocity perturbation (m/s)

α = Angle of incidence

ϵ = Atassi gust magnitude

ϕ = phase

ρ = Density (kg/m^3)

ζ = Wind tunnel correction factor

Accents and brackets

$\hat{}$ = Amplitude

$'$ = Value when distorted by potential field

$||$ = modulus

Subscripts

A = As modelled by Atassi

AS = Atassi function normalised by Sears quasi-steady lift

corr = Corrected for wind tunnel height

d = Distortion due to aerofoil

flap = Pertaining to the flaps

G = Gust

GM = Measured Gust

GP = Predicted Gust

QS = Quasi-steady

S = As modelled by Sears

∞ = Freestream quantity

I. Introduction

In many of the applications of fluid mechanics, it is necessary to know the unsteady load response of an aerofoil to a gust, but computing the response using a high-fidelity CFD code or undertaking detailed experimental analysis is often prohibitively expensive and time-consuming. For this reason, engineers tend to use analytical transfer functions,

which assume idealised behaviour of both the flow and the aerofoil. One such transfer function is the Sears function [1], which assumes a pure transverse gust (i.e. an incidence variation) interacting with a flat-plate aerofoil at zero mean incidence. The Sears-type gust is shown in Fig. 1(a): a uniform streamwise flow of velocity U_∞ and a transverse sinusoidal gust of amplitude $\hat{v}$ and reduced frequency k_1 encounters a flat plate at zero mean incidence, giving rise to an unsteady incidence variation $\hat{\alpha}_G$.

An extension to the Sears function was derived by Goldstein and Atassi [2][3]. The Atassi function models the flowfield shown in Fig. 1(b), which has a transverse gust similar to the Sears gust, but an additional streamwise gust of magnitude $\hat{u}$ and reduced frequency k_2 is introduced. Further to this, the Atassi function models an aerofoil with both camber and incidence and thus takes into consideration the coupling effect between the gust and the potential field of the loaded aerofoil. Recent work by Wei et al. [4] studied an unloaded aerofoil in a gust with both transverse and streamwise components. They showed that the Atassi function gives good agreement with wind tunnel data, and that in the absence of aerofoil loading (as is the case for their un-cambered aerofoil at zero angle of attack), the difference between the Sears and Atassi functions is simply a matter of normalisation. This is because the second order terms in the Atassi function are only present when the mean aerofoil load is non-zero, as will be discussed in Section II.

Given the increased applicability of the Atassi function over the Sears function, it is perhaps surprising that little work has been undertaken on its validation and limitations. Furthermore, wind tunnel facilities that aim to generate a Sears-type gust will often use a series of flaps, or louvres. These flaps will either introduce a vertical variation in the flow due to the wakes from the flaps (if they are closely spaced) or allow deviation of the flow far from the flaps, and thus a smaller gust amplitude than expected (if the flaps are spaced widely apart). If a vertical variation is introduced to the flow, the gust will resemble the flow modelled by Atassi as opposed to that modelled by Sears. Wei et al. [4] demonstrated the switch from Sears-type to Atassi-type flow by varying the flap spacing, while Jancauskas et al. [5] tested a gust generator with only two widely-spaced flaps and found generally good agreement with the Sears function.

As an alternative to using flaps to generate an unsteady inflow, Holmes [6] created a closed wind tunnel with flexible walls that could move either in or out of phase with each other. This enabled the generation of pure Sears-type (transverse) gusts, or pure Theodorsen-type (streamwise) gusts. The gusts could also be combined to give an Atassi-type flow. The work was undertaken prior to the advent of most modern unsteady flow measurement techniques and so information about the gusts themselves is sparse, but the results showed good agreement with the theoretical values for unsteady load amplitude.

One of the applications in which the Sears function can be used is the estimation of tidal turbine blade fatigue life [7]. In this paper, therefore, an aerofoil representative of a tidal turbine blade is used for the experiments. This aerofoil is thicker (21% chord) than those typically used in aerodynamics experiments, and has significant camber (2% chord). Some data of a loaded aerofoil encountering a harmonic gust was presented by Cordes et al. [8], who tested a cambered Clark-Y section at different angles of attack. However, it was later stated by Traphan et al. and Wei et al.

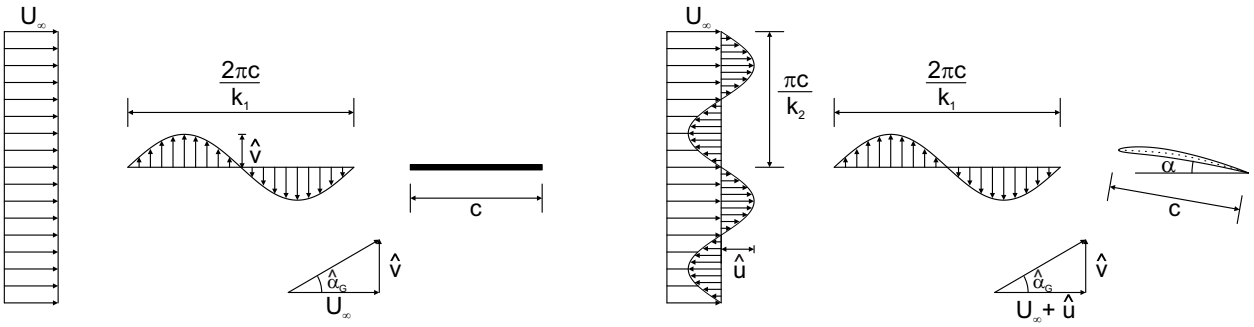

(a) Sears function.

(b) Atassi function.

Fig. 1 Sketch of the aerofoil gust encounters modelled by the Sears and Atassi functions, including the definitions of k_1, k_2 and $\hat{\alpha}_G$ used in this work.

that the gust in their facility varies substantially in the spanwise direction (i.e. the gust is three-dimensional) [9][4], and so the Atassi function would not be expected to apply.

The data shown in this paper therefore gives new information on how an aerofoil with camber and at non-zero angle of attack responds to an Atassi type gust. These are the conditions (i.e. when the aerofoil loading is non-zero) in which the Atassi function differs significantly from the Sears function, and so these experiments provide new insights into the flow behaviour.

The paper is structured as follows. After an overview of the Sears and Atassi functions, the experimental facility and method are described. The flowfield in the wind tunnel is examined under both steady and unsteady flow, with and without the aerofoil, with the aim of testing the assertion of Goldstein and Atassi that the incoming gust and the upstream aerofoil potential field will superpose linearly [2]. The physical definition of the Atassi gust and its relationship, or otherwise, to the flap wakes is then discussed and it is shown that the streamwise component of the gust is actually generated by a slight slanting of the wave front across the height of the wind tunnel. The unsteady lift measured in the experiments is then compared with the predictions of the Sears and Atassi functions, and the effects of both camber and incidence are examined. Some limits of agreement between the Atassi function and the experimental data are also found. Finally, an examination is undertaken of the propagation of the gust down each surface of the aerofoil, to see whether there is evidence of the gust being stretched on the suction surface due to the faster local flow, as asserted by Goldstein and Atassi [2].

II. The Sears and Atassi functions

A. Physical models

The Sears function [1] is used to find the unsteady lift caused on an aerofoil by a sinusoidal transverse gust, shown in Fig. 1(a). The function was derived assuming zero mean aerofoil loading (zero thickness, camber and mean angle of attack), but does not lose accuracy when applied to aerofoils with non-zero mean loading if the gust is purely transverse (i.e. with no k_2 component) [3]. The Atassi function was developed by Goldstein and Atassi [2][3] to account for the coupling effect between the mean aerofoil potential field and the gust, for gusts with both transverse and streamwise components (shown schematically in Fig. 1(b)).

The Sears function applies to gusts of the following form:

$$\mathbf{u} = \epsilon U_\infty \exp[i(k_1 x - k_1 t)]\mathbf{i} \tag{1}$$

The Atassi function applies to gusts with an additional harmonic streamwise component. These gusts therefore take the form:

$$\mathbf{u} = (\hat{u}\mathbf{i} + \hat{v}\mathbf{j}) \exp[i(k_1 x + k_2 y - k_1 t)] = \epsilon U_\infty \left(-\frac{k_2}{|k|}\mathbf{i} + \frac{k_1}{|k|}\mathbf{j}\right) \exp[i(k_1 x + k_2 y - k_1 t)] \tag{2}$$

Here, $|k|$ is defined as $\sqrt{k_1^2 + k_2^2}$. The aerofoil is assumed to be aligned with the horizontal axis, so the **j**-vector represents the transverse gust component, and the **i**-vector the streamwise component. The definitions of k_1 and k_2 are given in Fig. 1.

The notable difference between the Sears gust (Eq. 1) and the Atassi gust (Eq. 2) is the definition of gust amplitude. In the case of the Sears gust, the amplitude is given by the variation in angle of attack, i.e.:

$$\hat{\alpha}_g = \epsilon U_\infty \tag{3}$$

For the Atassi gust, the gust amplitude is a function of both gust components. Given that the gust amplitudes are small ($\hat{u} << U_\infty, \hat{v} << U_\infty$), Wei et al. [4] showed that the amplitude of the oscillating inflow angle is given by:

$$\hat{\alpha}_g = \tan^{-1}\left(\frac{\epsilon U_\infty \frac{k_1}{|k|}}{U_\infty + \epsilon U_\infty \frac{k_1}{|k|}}\right) \approx \frac{\epsilon k_1}{|k|} \tag{4}$$

This means that for a fixed gust strength ϵ in Atassi's definition, and for nonzero k_2, the actual measured variation in angle of attack $\hat{\alpha}_g$ will increase with k_1. As noted by Wei et al., "the gust strength [ϵ] in the Atassi problem is not strictly tied to the physical quantity [the gust angle $\hat{\alpha}_g$]" [4].

The dependence of the gust amplitude on the harmonic frequencies k_1 and k_2 in Eq. 4 is a consequence of continuity. From the definition of velocity in Eq. 2 the continuity equation becomes:

$$\frac{du}{dx} + \frac{dv}{dy} = ik_1\hat{u}\exp[i(k_1x + k_2y - k_1t)] + ik_2\hat{v}\exp[i(k_1x + k_2y - k_1t)] = 0 \tag{5}$$

Cancelling out equal terms in Eq. 5 gives:

$$k_1\hat{u} + k_2\hat{v} = 0 \tag{6}$$

This means that the transverse and streamwise gust amplitudes must change in response to changes in the reduced frequencies k_1 and k_2. The definitions of $\hat{u}$ and $\hat{v}$ given in Eq. 2 satisfy continuity through Eq. 6. This analysis demonstrates that the frequency-dependent definition of the gust amplitudes used by Atassi in Eq. 2 is appropriate and has a physical origin.

B. Transfer functions

In order to obtain the unsteady lift amplitude from the transfer functions, in response to the unsteady gusts in Eq. 1 and 2, the transfer functions are multiplied by the quasi-steady lift, $\hat{L}_{\text{QS}}$. The Sears function gives the unsteady lift as:

$$\hat{L}_{\text{S}} = S(k_1)\left(\hat{L}_{\text{QS}}\right)_{\text{S}} \tag{7}$$

where $S(k_1)$ is the Sears transfer function. The Atassi function gives the lift as a combination of the Sears transfer function and two additional terms:

$$\hat{L}_{\text{A}} = \left[S(k_1)\frac{k_1}{|k|} + \alpha\hat{L}_{\alpha}\left(k_1, k_2\right) + m\hat{L}_{m}\left(k_1, k_2\right)\right]\left(\hat{L}_{\text{QS}}\right)_{\text{A}} \tag{8}$$

The second and third terms in Eq. 8 are both zero if k_2 is zero. The second term relates to the steady angle of attack, α, in radians, and the third to aerofoil camber, m, as a fraction of the aerofoil chord length. The expressions $\hat{L}_{\alpha}\left(k_1, k_2\right)$ and $\hat{L}_{m}\left(k_1, k_2\right)$ are complicated functions of the gust frequencies, and can be found in the original work [3].

A recent study by Wei et al. [4] investigated the differences between Sears-style and Atassi-style gusts, and carried out experimental validation of both transfer functions for a thin symmetric aerofoil at zero mean angle of attack. This means that no aerofoil loading was included in the analysis, and any difference in load response between the Sears and Atassi gusts was due to the nature of the gust – whether or not it had a significant k_2 component. Wei et al. provide valuable insight into the Atassi function, showing that one of the primary differences from the Sears function is its definition of quasi-steady lift, $(\hat{L}_{\text{QS}})$. In the Sears function the quasi-steady lift is given as a function of the gust amplitude, as:

$$\left(\hat{L}_{\text{QS}}\right)_{\text{S}} = 2\pi\rho c U_\infty \hat{v} \approx \pi\rho c U_\infty^2 \hat{\alpha}_{\text{g}} \tag{9}$$

For the Atassi function, the quasi-steady lift is instead given by:

$$\left(\hat{L}_{\text{QS}}\right)_{\text{A}} = \pi\rho c U_\infty^2 \epsilon \tag{10}$$

In this case, the gust amplitude is defined by the gust strength parameter ϵ. Wei et al. showed that ϵ and $\hat{\alpha}_{\text{g}}$ are related through Eq. 4, showing that the difference between the quasi-steady lift as defined in the Sears and Atassi functions lies in the factor $k_1/|k|$. Wei et al. went on to show that for a symmetric aerofoil at zero mean angle of attack, the Atassi function was equivalent to the Sears function if multiplied by $|k|/k_1$, for any value of k_2.

As explained by Atassi [3] and by Wei et al. [4], significant differences between the Sears and Atassi functions only emerge when there is *both* a k_2 component in the gust, *and* non-zero mean aerofoil loading due to camber or angle of attack. An example of a case where the Atassi and Sears functions give significant differences in response is given in Fig. 2(a). This figure shows the response functions obtained from the Sears and Atassi functions, for an aerofoil with 2% camber and 3° mean angle of attack, undergoing oblique gust forcing ($k_1 = k_2$). The response function is defined as follows for the Sears function:

$$R_{\text{S}} = \frac{\hat{L}_{\text{S}}}{\left(\hat{L}_{\text{QS}}\right)_{\text{S}}} = S(k_1) \tag{11}$$

while for the Atassi function it is given by:

$$R_{\text{A}} = \frac{\hat{L}_{\text{A}}}{\left(\hat{L}_{\text{QS}}\right)_{\text{A}}} = S(k_1)\frac{k_1}{|k|} + \alpha\hat{L}_\alpha\left(k_1, k_2\right) + m\hat{L}_m\left(k_1, k_2\right) \tag{12}$$

In order to show a more direct comparison between the Sears and Atassi functions, a third response function is defined by multiplying the Atassi function by $|k|/k_1$, thus normalising it by the same quasi-steady lift as is used in the Sears function:

$$R_{\text{AS}} = \frac{\hat{L}_{\text{A}}}{\left(\hat{L}_{\text{QS}}\right)_{\text{S}}} \tag{13}$$

In order to illustrate the differing contributions of the incidence and camber effects, the functions $\hat{L}_\alpha\left(k_1, k_2\right)$ and $\hat{L}_m\left(k_1, k_2\right)$ are shown separately in Fig. 2(b) for the same aerofoil and gust conditions.

Unlike the work of Wei et al. [4], the experiments undertaken in this work use an aerofoil with camber at nonzero angles of incidence. This will test the assertion that it is only in the presence of both a vertical (k_2) gust component and non-zero mean aerofoil loading that the results differ significantly from the Sears function.

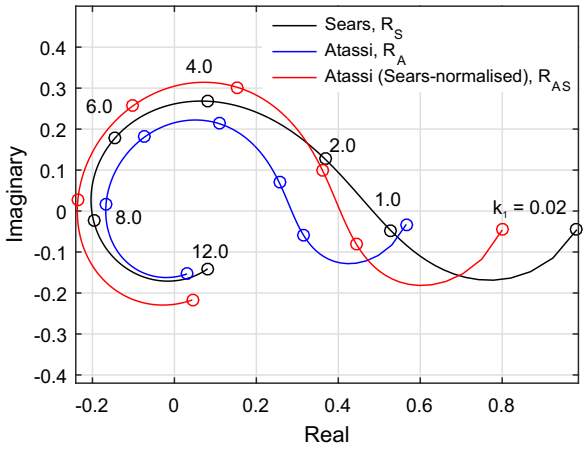

(a) Comparison of Sears and Atassi response functions.

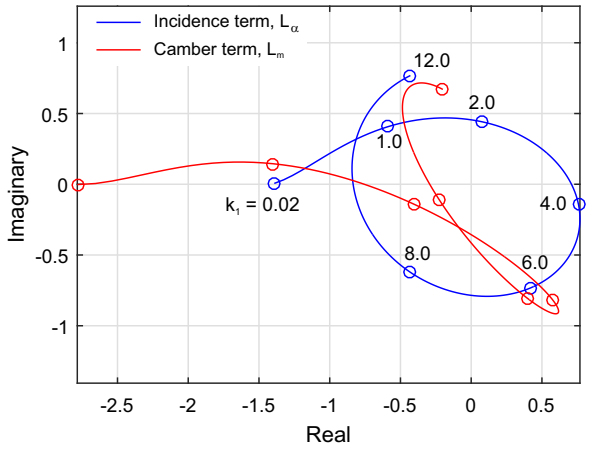

(b) Camber and incidence terms for the Atassi function.

Fig. 2 Example Sears and Atassi response functions for an oblique gust ($k_1 = k_2$) interacting with an aerofoil with 2% camber at 3°aerofoil incidence.

Parameter	Value
Tunnel height (m)	1.00
Flow speed (m/s)	18.0 - 26.0
Aerofoil chord (m)	0.115
Aerofoil aspect ratio	2.96
Aerofoil Reynolds number	1.41 - 2.08x10^5
Number of flaps	58
Flap chord (mm)	35
Flap frequency range (Hz)	0 - 8
Reduced frequency range	0 - 0.35

Table 1 Key parameters of the wind tunnel

III. Experimental Method

Schematics of the wind tunnel are shown in Fig. 3(a) and (b), alongside a photograph of the wind tunnel in Fig. 3(c). The key parameters of the tunnel are given in Table 1. The working section has solid side walls but is open at the top and bottom, to allow the flow to turn freely as it passes over the aerofoil. A 2D NACA aerofoil is mounted at mid-height and two chords downstream of the tunnel inlet. The aerofoil profile was chosen to be representative of a tidal turbine aerofoil, and so has moderate camber (2% chord) and is relatively thick (21% chord). The aerofoil is mounted on a turntable in order to vary the angle of attack without moving the position of the leading edge in the tunnel. Circular fillets of radius 3% span were fitted at the junction between the aerofoil and the wind tunnel endwalls. These fillets were found to suppress the endwall corner separation and prevent it from affecting the flow over the majority of the aerofoil span, thus giving the desired 2D flow at mid-span. Upstream of the working section there are a vertical series of flaps which are designed to control the angle of the flow as it exits the wind tunnel. The flap cross-section is a NACA-0012. The flaps are extruded Aluminium, and on both surfaces of each flap there is a carbon-fibre stiffener of

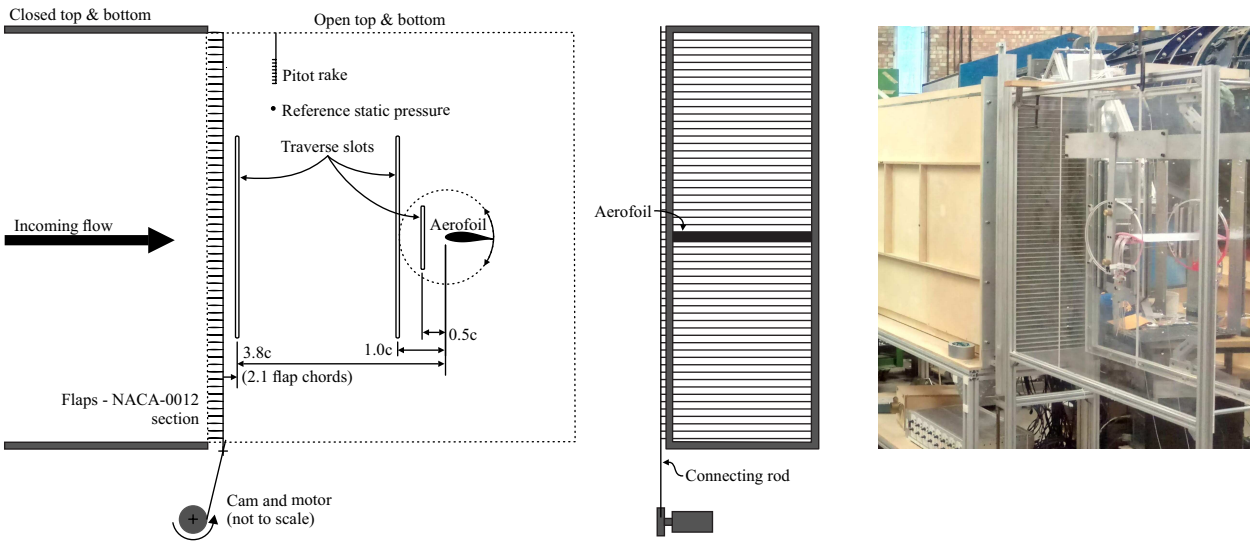

(a) Side view.

(b) End view (flow out of page).

(c) Photograph from downstream.

Fig. 3 Diagrams and photograph of the wind tunnel test facility.

thickness 0.5 mm. The stiffeners prevent spanwise bending of the flap and were not found to have an adverse effect on the flow quality downstream of the flaps. The flap chord was chosen as a balance between the need for stiffness (which sets a minimum thickness) and the desire to minimise unsteady flow behaviour of the flaps (the reduced frequency of the flap motion will be related to the reduced frequency of the gust encountered by the main aerofoil by $k_{\text{flap}} = k_1 c_{\text{flap}}/c$).

The decision of how many flaps to install was made by considering the theoretical case of an infinite number of flaps with infinitesimal loading. In this case, the flaps would generate a continuous vortex sheet as envisaged by Sears. The flaps were therefore packed as tightly as possible which gave a ratio of 0.5 between the flap chord and the vertical spacing of the flaps. Placing the flaps further apart would also risk introducing flow deviation away from the flap surfaces.

The flaps are mounted in bearings on an Aluminium frame and attached to a DC motor via a cam and a connecting rod. The mechanism can therefore generate a sinusoidal variation in flow incidence similar to the Sears-type gust. The amplitude of the gust can be varied by changing the cam size, and the frequency is adjusted by changing the speed of the motor. For steady-state tests, the flaps are held in either their fully up or fully down position.

The tunnel operating conditions are measured using a sidewall static pressure tapping and a rake of Pitot probes between the flaps and the aerofoil, as shown on Fig. 3(a). The reference velocity from these probes is within 1% of the average inlet velocity integrated over the central portion of the wind tunnel. The incoming flow has a turbulence intensity of approximately 0.5%.

The aerofoil pressure distribution is measured using 43 aerofoil surface pressure tappings at midspan. The tappings are connected to fast-response pressure transducers via a set of semi-infinite lines. The use of semi-infinite lines

enables high-frequency measurements to be taken in confined spaces by removing the requirement for the transducers to be mounted on the aerofoil surface [10]. For the work described in this paper, 1 mm bore tubing was used and a 1 m length was used between each tapping on the aerofoil surface and a 3-way connection. From the 3-way connector, a short (<10 cm) length went to each transducer and a long (30 m) length was open to the atmosphere. With the semi-infinite lines connected, the amplitude and phase of the response changes with frequency and so the tappings with semi-infinite lines were calibrated against a surface-mounted fast-response transducer using a signal generator and a loudspeaker. In these tests, the resonant frequency of the tappings was found to be over 200 Hz, which is above the range of frequencies of interest in this work. For steady state tests, the tappings are connected to the transducers without the semi-infinite lines.

An unsteady total pressure probe was traversed vertically through the flow at various axial locations upstream of the aerofoil (see Fig. 3(a) for the positions). By measuring the flow three times with the probe oriented at three angles (-45°, 0°, +45°) the equivalent data from a fast-response three-hole probe could be reconstructed and thus the flow angle and speed could be calculated. This enabled the gust to be characterised in space and time both with and without the aerofoil installed. The error in the peak-to-peak gust magnitude measured using this method is approximately ±0.25°, which is small in absolute terms but large relative to some of the gusts, as will be discussed in Section VI.

Data were sampled at 20 kHz for 20-30 seconds depending on the frequency of the flaps. All data were phase-locked to the motor frequency using a once-per-revolution sensor on the shaft. This enabled the harmonic response to be averaged over 50-150 cycles.

IV. Steady-state behaviour of the aerofoil

The wind tunnel generates a finite jet with a height of approximately 8 times the aerofoil chord. This means that the aerofoil will behave slightly differently to an aerofoil in an ideal, infinite flow, as explained by Brooks et al. [11][12][13]. The most obvious consequence of the finite jet is that the lift is lower than expected and thus the lift curve does not follow the ideal $2\pi\alpha$ rule. This can be rectified by dividing the apparent angle of attack by a correction factor ζ. Correlations for ζ were developed for a zero-camber aerofoil by Brooks et al. [11][12]. For the aerofoil used in this work, the correction factor was found to be 1.19, which agrees with their correlation. In tests with a larger aerofoil (which will be discussed briefly in Section V), however, the correlation was found to be 5% higher than the value given by Brooks et al. This may be due to the fact that the aerofoil used in this work has non-negligible camber and thickness.

Steady-state measurements of aerofoil lift were made with the flaps at the working section inlet in both the 'up' and 'down' positions, such that the true incidence was:

$$\alpha_{\text{corr}} = \frac{\left(\alpha - \alpha_{\text{flap}}\right)}{\zeta} \tag{14}$$

A graph of lift coefficient against incidence corrected using Eq. 14 with the flaps in two positions is shown in Fig. 4(a). The data from the wind tunnel is compared with results from MSES (a coupled Euler-boundary layer solver [14]). It can be seen that both the flaps up (blue) and flaps down (red) data follow the same line with gradient 2π as the MSES prediction (black line) at angles below the stall angle. The errors in C_{L} are estimated to be smaller than the markers in Fig. 4(a), and the agreement between the two sets of data with the flaps in the up and down positions supports this assertion. The stalling behaviour of the aerofoil differs between MSES and the experiments; this is due to the large blockage generated when the aerofoil is at angles far from zero and the presence of aerofoil-endwall corner separations at high incidence. From this point onwards, all incidence values given for experimental data have been corrected using Eq. 14.

The reason for the reduction in lift in a finite jet is explained by Brooks et al. [11] as being due to the restriction of the aerofoil potential field: there is a condition of zero velocity potential at the jet boundary and so the aerofoil can be considered to be in an infinite cascade. The correction found above will only match the total aerofoil lift - the surface pressure distribution will still be different in the finite jet case, and the potential field around the aerofoil will not match.

For the aerofoil considered here, the error in pressure distribution is quite small. This is shown in Fig 4(b), where the measured surface pressure (dots) is compared with data from MSES (solid lines) at three different incidences. It can be seen that there is good agreement between the simulations and the experiments. This is may be due to fact that the jet height ratio of 8 used in this work is towards the upper end of those used in the literature (Brooks et al. [13] undertook tests with jet ratios from 0.5 to 11).

The aerofoil potential field will distort an incoming vortical gust, due to the differing convection speeds in different parts of the flow field, and this may affect the resulting unsteady load, as modelled by Goldstein and Atassi [2]. In the case of a Sears-type gust, the potential field and the gust will behave independently, but Atassi [3] argues that the presence of vertical non-uniformities in the gust will cause coupling between the gust and the potential field. Goldstein and Atassi [2] state that the incoming gust and potential field will superpose linearly, but that the gust convection speed will be different across the two surfaces of the aerofoil (in contrast to the frozen gust hypothesis, which is valid for an un-loaded aerofoil). This difference in convection speed is what causes the discrepancy between coupled and uncoupled gust response. These points will be discussed in the next three sections.

V. Unsteady gusts and their interaction with the aerofoil potential field

The flow angle variation due to the aerofoil potential field is shown in Fig 5(a), which is taken from an MSES simulation in infinite flow at zero angle of attack. As expected, the most substantial changes in flow angle are close to the aerofoil, but the aerofoil also exerts a non-negligible influence on the upstream flow. To see this more clearly, the change in flow angle relative to the mean incidence is shown in Fig. 5(b); this distortion is defined as α_{d}. The data is taken from 0.5 chords upstream of the aerofoil and from simulations at incidences from -8° (black) to +4° (red).

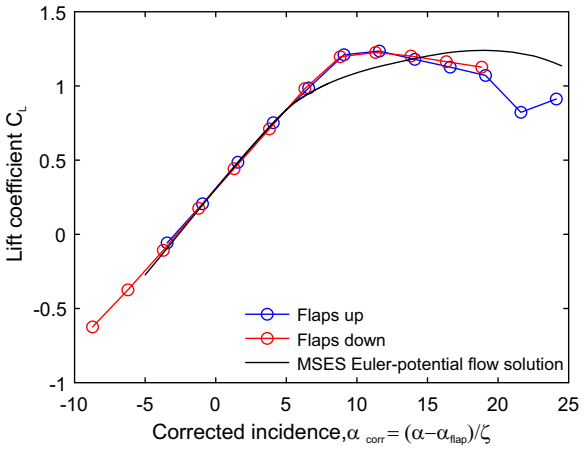

(a) Lift coefficient against corrected incidence.

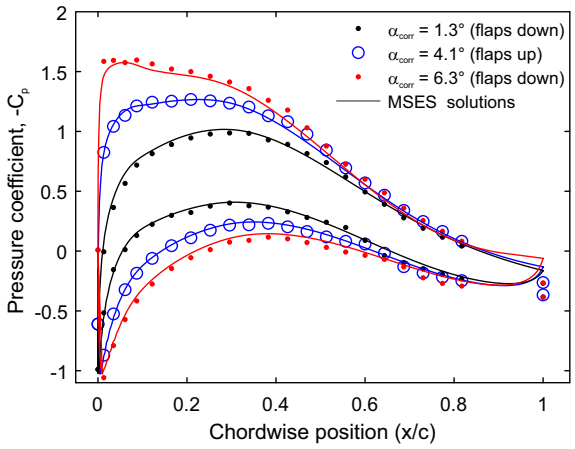

(b) Surface pressure distributions with the aerofoil at three different incidences.

Fig. 4 Lift curve and surface pressure distributions from MSES and experimental data showing good agreement when the wind tunnel correction factor is applied to the incidence.

Distortions of up to 4° from the mean incidence are observed, with the flow being deflected up on the top surface of the aerofoil and down on the bottom surface. The distortion in the flowfield is not linear with average incidence or with vertical position, and the maximum distortion increases with aerofoil loading.

The flow angle measured in the wind tunnel with the aerofoil in place will be affected by this distortion. If the assertion of Goldstein and Atassi [2] is correct, then the measured distorted gust, α'_{GM}, will be the sum of the gust measured in the empty wind tunnel α_G and the distortion due to the quasi-steady aerofoil potential field, α_d. The quasi-steady distortion, α_d, can be found from the data shown in Fig. 5(b), by interpolating for the measured empty-tunnel incidence (this interpolation is done after the wind tunnel correction factor, ζ, has been applied to the empty tunnel data). We denote this predicted gust incidence as α'_{GP}:

$$\alpha'_{GP} = \alpha_G + \alpha_d \tag{15}$$

Figure 6 shows the incidence variation (flow angle) measured by a probe 0.5 chords upstream of the aerofoil with the aerofoil in place at a nominal incidence of 0°*, α'_{GM}, (black lines). The same data is alsow shown from the empty wind tunnel measurements, α_G, (blue) and for the predicted distorted gust, α'_{GP}, as defined in Eq. 15 (red).

Figure 6(a) shows the flow angles with flaps stationary in two different positions. Considering first the empty wind tunnel data (blue), it can be seen that with the flaps in the 'up' position, the flow angle oscillates around a mean of approximately -0.4°, while the angle reduces to -5.8° when the flaps are moved to the 'down' position. In both cases, the wakes from the flaps are visible, causing a 1-2° variation in flow angle, but the mean angle over each flap pitch remains constant between the top and the bottom of the traverse. When the aerofoil is in the wind tunnel, the measured angle, α'_{GM}, is indeed different from α_G. As expected from Fig. 5, the effect of the aerofoil potential field is different

*This corresponds to a corrected mean incidence of -3.2°, using Eq. 14

at the two mean incidences shown in Fig. 6(a): in the flap up case, the incidence is increased at positions above the aerofoil and reduced slightly below the aerofoil, while the flap down case shows a large reduction in incidence below the aerofoil, reducing to nothing at the top of the measurement plane. The trend in the predicted flow, α'_{GP} (shown in

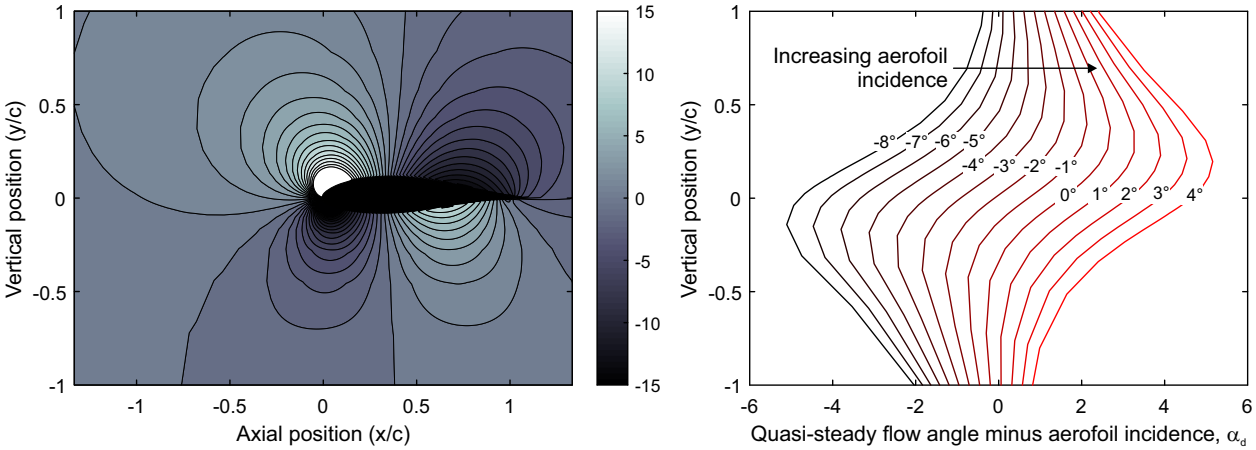

(a) Flow angles round the aerofoil at zero incidence.

(b) Distortion angle against vertical postion at x/c = -0.5.

Fig. 5 Data from MSES simulations showing the effect of the aerofoil potential field on the incoming flow angle.

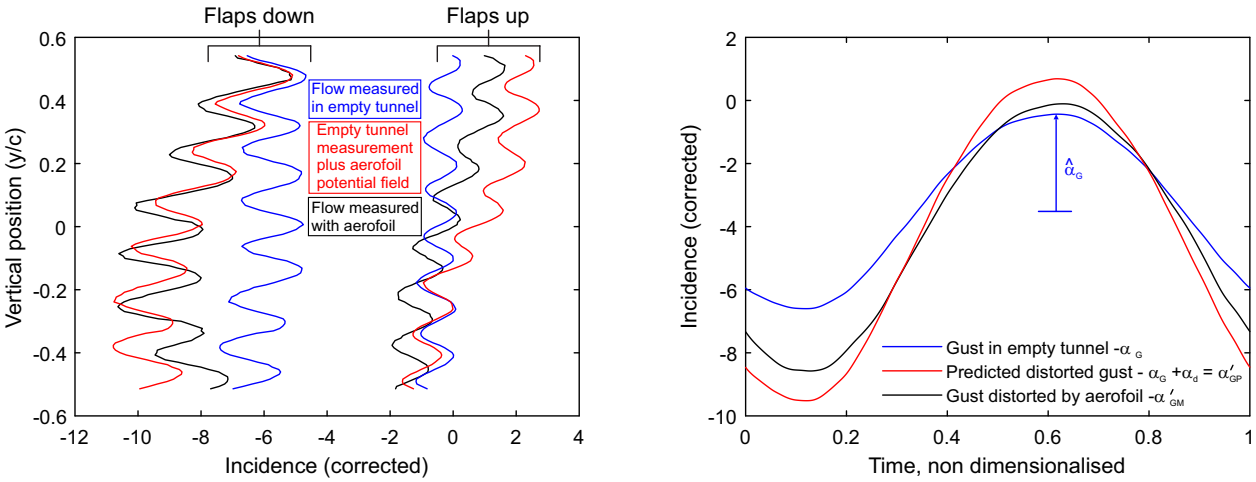

(a) incidence against vertical position for steady-state flow with the flaps in two positions.

(b) Incidence against time for a gust with reduced frequency k = 0.13.

Fig. 6 Traverses at x/c = -0.5 with the flaps in the up and down position showing the effect of the aerofoil on the steady-state flow compared with the no-aerofoil case superposed on the predicted potential field from MSES.

red), is approximately correct, but the magnitude of the distortion is over-predicted. This is particularly apparent in the data from the top half of the traverse plane with the flaps up, where the distortion predicted by MSES, α_d (the difference between the blue and red lines), is approximately twice the size of the measured distortion (the difference between the blue and black lines). When averaged over the traverse plane, α'_{GP} for the flaps up case is 1.0° higher than the measured angle, α'_{GM}, while the difference in the flaps down cases is 0.2° (this smaller value is within the experimental error bounds). This discrepancy between the distortion predicted by MSES and the measured data suggests that the aerofoil

potential field is, indeed, affected by the boundaries of the finite jet, despite the agreement of the surface pressure distributions with MSES (Fig. 4(b)).

The effect of finite jet height on the upstream potential field has not been studied in much detail, perhaps due to the historically greater difficulty in measuring the flowfield as opposed to the aerofoil forces and pressure distribution. A CFD study was conducted by Moreau et al. [15], in which they compared the potential field of an aerofoil in an infinite jet with those obtained with finite height to chord ratios of 1.0 and 3.8. Their results show qualitatively that the incoming flow behaves differently as the jet height changes but they do not suggest any means of correcting for this effect.

When the flaps are moving, a similar gust distortion is observed to that discussed above, i.e. the gust is larger when the aerofoil is installed than in the empty wind tunnel case. An example of this is shown in Fig. 6(b), which shows the gusts generated by the flaps at a reduced frequency, k_1, of 0.13. The data is taken from the same traverse plane as Fig. 6(a) and the incidence has been averaged over the whole vertical range at each time-step.

The moving flaps generate a sinusoidal gust, resulting in time-warying incidence. The blue line in Fig. 6(b) gives the gust amplitude, $\hat{\alpha}_G$, needed for normalising the Sears and Atassi response functions (Eq. 3 and 4). With the aerofoil in place at a nominal incidence of 0° (black line)[†], the gust is distorted such that the minimum incidence is reduced by approximately 2° while the maximum incidence increases by under 0.5°. The gust also deviates from a perfect sinusoid, with a slight skewing of the peak to a later time than that in the empty tunnel case. The predicted distorted gust, α'_{GP} (Eq. 15) is shown in red. Both the increase in gust magnitude and the skewing of the peak are predicted by this superposition. As in the steady case, however, the amplitude of the gust is over-predicted relative to the measured data.

Gusts of three different amplitudes were generated at a variety of reduced frequencies from 0 (steady) to 0.35, and the gust was measured with and without the aerofoil in place at its nominal zero incidence as in Fig. 6(b). The peak-to-peak amplitude of the predicted distorted gust ($2\hat{\alpha}'_{GP}$) is plotted against the actual gust amplitude measured with the aerofoil in place ($2\hat{\alpha}'_{GM}$) in Fig. 7(a). The data points from this set of tests are shown in red, with different markers denoting each reduced frequency. The dotted black line denotes exact agreement between the measured and predicted gusts ($\hat{\alpha}'_{GP} = \hat{\alpha}'_{GM}$), while the solid black line shows a straight line through the red points which has equation $\hat{\alpha}'_{GP} = 1.18\hat{\alpha}'_{GM}$. The error between the predicted and measured gust size is shown in Fig. 7(b), where it can be seen that it is between 10 and 20% for all but one case. This data therefore shows that the difference between the gust distortion predicted by MSES and that measured in the wind tunnel is independent of gust amplitude or frequency. These results suggest that the superposition of the two flowfields is linear and is not affected by unsteady coupling over the frequency range tested.

The effect of reduced frequency on the amplitude of the gust both with and without the aerofoil is shown more

[†]This corresponds to a corrected mean incidence of -3.2°, using Eq. 14

clearly in Fig. 8(a), which is a plot of incidence change against reduced frequency for the cases with the largest cam (which gives a peak-to-peak incidence variation of just under 6° in the empty wind tunnel case - Fig. 6). Considering first the blue markers, which show the data from the empty wind tunnel, there appears to be a slight increase in gust amplitude with reduced frequency (though the changes are of a similar size to the experimental error). This is in line Eq. 4, which shows the dependence of gust amplitude on k_1. Wei et al [4] saw a more marked increase in amplitude with reduced frequency in their tests; this is likely to be due to the higher streamwise gust frequency, k_2, in their tests. The actual gust amplitude (black markers) follows the same trend as the empty tunnel results. When the empty gust data is superposed with the potential field from MSES, the data represented by the red markers are obtained. The gap between the blue and black markers remains approximately constant with reduced frequency, suggesting that there are no unsteady effects in the superposition of the incoming gust with the aerofoil potential field.

The average error of 18% between the predicted and measured gust amplitude is very close to the wind tunnel incidence correction factor discussed in Section IV, which is 1.19. This adjustment has, however, already been taken into consideration in the calculations shown in Fig. 7(a). Also shown on Fig. 7(a) are three measurements taken with a larger aerofoil of 230 mm chord (blue)[‡]. The wind tunnel correction factor for this aerofoil is 1.51, but the data lies on the same line as that from the smaller aerofoil, with an average error of 18%, and so the error appears not to be directly related to the ratio of wind tunnel height to aerofoil chord.

If the aerofoil incidence is changed, the quasi-steady potential field will change, as shown in Fig. 5(b). The effect of this on the superposition of the gust with the potential field was investigated by measuring the gust with the aerofoil at four different angles. The results of this are shown in Fig. 8(b), which is a plot of peak-to-peak amplitude change against aerofoil incidence for the gust with a reduced frequency, k_1 of 0.13 shown in Fig. 6(b). Restrictions in the traverse slot arrangement meant that the flowfield had to be measured further upstream of the aerofoil (1.0 chords instead of 0.5 chords), and so the overall distortion is lower than in the other cases. Nevertheless, the same trend is observed - the blue line shows the magnitude of the gust in the empty wind tunnel, while the black squares show the gust with the aerofoil in place at each incidence. There is very little change in the distortion of the gust by the aerofoil across the incidence range tested, despite the lift coefficient changing by approximately 0.4 over this range. As with all the previous data, the prediction from superposing the simulated quasi-steady potential field with the empty-tunnel gust (red squares) gives a larger amplitude than the actual data.

The data from the cases with varying aerofoil incidence is denoted by the green stars on Figs 7(a) and (b). It can be seen that the error is consistent with all the other cases, suggesting that aerofoil incidence does not affect the superposition of the gust with the potential field (at least for attached flow). Taken as a whole, the data in Figs 7 and 8 show that the gust and the aerofoil potential field superpose linearly regardless of gust reduced frequency, aerofoil chord and angle of attack. There is a consistent error between $\hat{\alpha}'_{\text{GP}}$ (the prediction obtained by addition of the simulated

[‡]This data is taken from 0.5 chords upstream of the larger aerofoil, i.e. twice as far away in absolute terms.

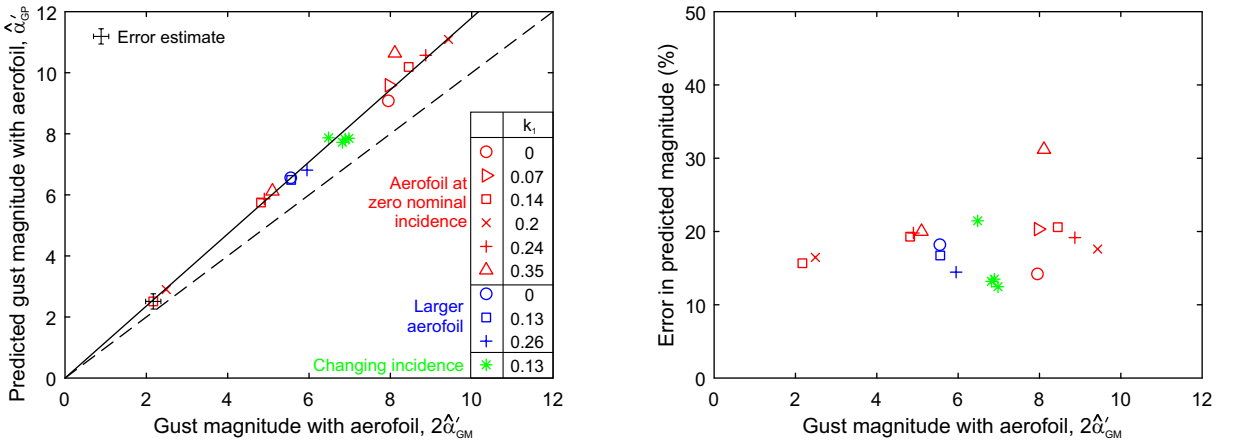

(a) Predicted gust magnitude against measured gust magnitude with aerofoil.

(b) Error in predicted gust magnitude against measured gust magnitude with aerofoil.

Fig. 7 Measured flow angles at x/c = -0.5 with and without the aerofoil in place, compared with the angles obtained by adding the no-aerofoil data to the simulated aerofoil potential field from Fig. 5(b).

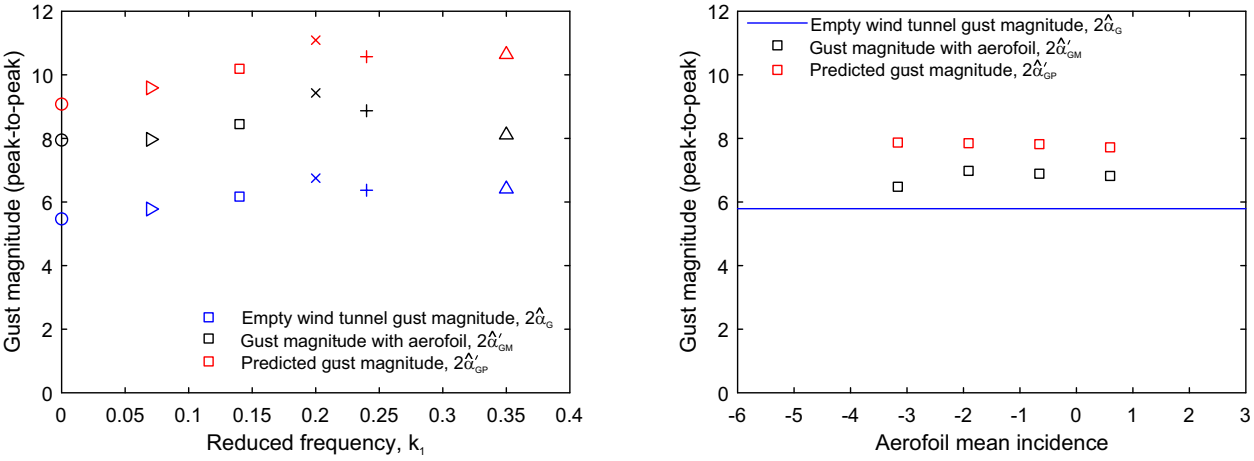

(a) Gust magnitude against reduced frequency, k_1.

(b) Gust magnitude against aerofoil mean incidence.

Fig. 8 Effect of reduced frequency and aerofoil mean incidence on the magnitude of the gust in the empty wind tunnel and with the aerofoil in place (both predicted and measured).

quasi-steady field to gust measured in the empty wind tunnel) and $2\hat{\alpha}'_{GM}$, (the gust measured with the aerofoil in place), but the fact that the error is unaffected by the magnitude of the aerofoil potential field or by the reduced frequency shows that there is no non-linear coupling of the two flowfields upstream of the aerofoil over the range of variables tested here.

The finding that the gust distortion is independent of reduced frequency is in line with the theory of Goldstein and Atassi [2], who state that the incoming gust will not have its amplitude changed by the steady-state flowfield. Goldstein and Atassi do state, however, that the wavelength of the gust will change over the aerofoil chord, and this will be discussed briefly in Section VII. Now that the gusts generated have been quantified, the aerofoil lift response will be compared with that predicted by the models of Sears and Atassi.

VI. Aerofoil lift response

A. Measuring unsteady lift

The unsteady component of lift was found by direct integration of the Fourier coefficients, A_N and B_N, for each surface pressure measurement at the gust frequency, f_{gust}:

$$A_N = \frac{2}{M}\int_0^M P(t)\sin\left(2\pi f_{gust}t\right)dt; \tag{16}$$

$$B_N = \frac{2}{M}\int_0^M P(t)\cos\left(2\pi f_{gust}t\right)dt; \tag{17}$$

where $P(t)$ is the pressure signal and M is the length of the sample (which was set to be many gust cycles, see Section III). The two Fourier coefficients combine to give the phase and amplitude of the response at each location (once a calibration has been applied to take into account the phase lag and attenuation due to the semi-infinite lines). The unsteady pressure difference is then integrated along the aerofoil chord to give the lift. This measured value of unsteady lift can then be compared with the load predicted by the Sears and Atassi functions.

B. Calculating k_2 and ϵ

The frequency of the streamwise gust component, k_2, has a significant impact on the result of evaluating the Atassi function. This means that it is vital to obtain an accurate estimate of k_2 when comparing experimental results with the Atassi function. It is tempting to estimate the spatial frequency in the vertical plane from Fig. 6(a) and the definition of k_2 given in Fig. 1(b). By this process, k_2 appears to be approximately 20. However, this method of visually estimating k_2 from the wake spacing in Fig. 6(a) may not be appropriate, as there is no guarantee that the gust corresponds to the ideal Atassi gust as defined in Eq 2. Instead, the more accurate approach of Wei et al. [4] should be taken and k_2 and ϵ must be calculated from the measured values of k_1 and $\hat{\alpha}_G$ via a two-parameter fit to Eq. 4. The results of this two-parameter fit for k_2 and $\hat{\alpha}_G$ are shown in Fig. 9.

Figure 9(a) shows the relationship between the gust amplitude parameter, ϵ and measured gust amplitude $\hat{\alpha}_G$. It can be seen that ϵ increases linearly with $\hat{\alpha}_G$, as would be expected from Eq. 4. Figure 9(b) shows the calculated k_2 values (blue stars), against measured gust amplitude, $\hat{\alpha}_G$. The measured ranges of k_1 are included in red for comparison. Figure 9(b) shows that k_2 is reduces slightly with increasing gust amplitude, and that it has a mean value of 0.035. The two-parameter fit method therefore gives a significantly lower value of k_2 than that which was calculated from the visual estimate of k_2 from Fig. 6(a).

The effect of k_2 on the physical nature of the gust can be seen by visualising the Atassi function. Figure 10 shows space-time contour plots of flow angle for gusts with the same k_1 but different values of k_2. On the x-axis

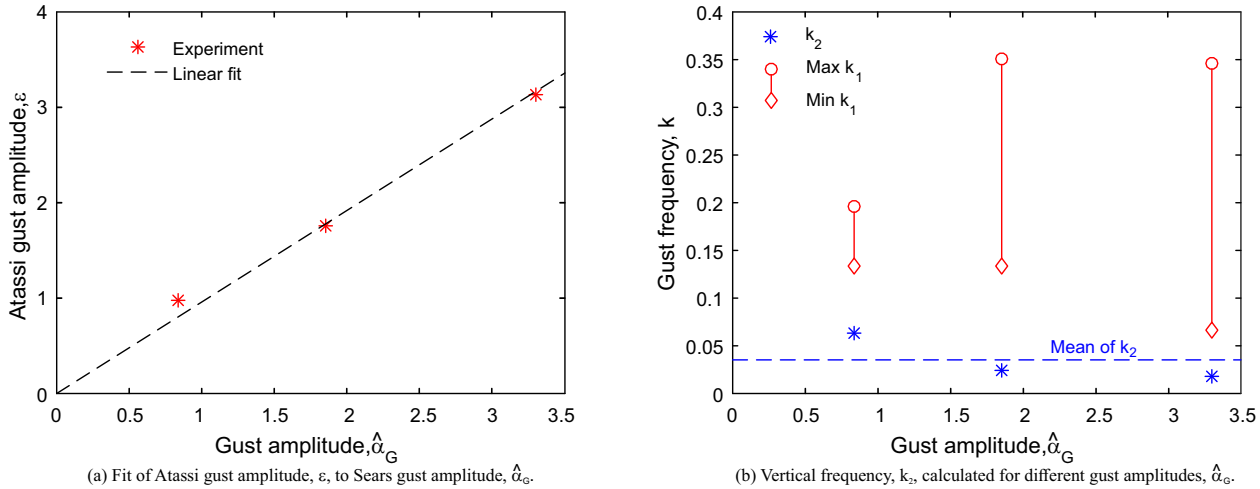

(a) Fit of Atassi gust amplitude, ε, to Sears gust amplitude, $\hat{\alpha}_G$.

(b) Vertical frequency, k_2, calculated for different gust amplitudes, $\hat{\alpha}_G$.

Fig. 9 Results of the two-parameter fit for ϵ and k_2 from measured values of $\hat{\alpha}_G$ and k_1.

is non-dimensional time, while the y-axis is vertical position and the contours normalised by the gust amplitude, $\hat{\alpha}_G$. Figures 10(a) and (b) show the ideal Atassi gust obtained from Eq. 2, while Fig. 10(c) is experimental data from the empty wind tunnel (1 chord upstream of the aerofoil position). It can be seen that the value of k_2 makes a marked difference to the physical shape of the gust. The gust in Fig. 10(a) corresponds to $k_2 = 0.035$ (the value from the two-parameter fit), while the higher value of $k_2 = 20$ from the visual estimate is used in Fig. 10(b). At low values of k_2 (Fig. 10(a)), the gust is almost uniform over the whole vertical range of the plot, so the flow almost exactly resembles a Sears-type gust. As k_2 is increased, the wave front becomes shifted in phase at different vertical locations (Fig. 10(b)). When k_2 is very high (Fig. 10(b)), the gust front is slanted to such an extent that the gust repeats with a very short wavelength in the vertical direction.

Considering now the space-time plot for the measured gust (Fig. 10(c)), the wave front is visually most similar to the ideal low-k_2 gust in Fig. 10(a). The effect of the flap wakes is to introduce a small spatial variation along the vertical axis, but this appears as a stationary disturbance, and the main wave front is not significantly slanted. This result provides visual confirmation that the two-parameter fit is the appropriate method for determining k_2.

The finding that k_2 is determined by the angle of the wave front as opposed to the flap spacing suggests that the flap wakes are not the cause of the "Atassi component" of the gust. It is more likely that there is a variation in the vertical direction due to a slight asymmetry in the wind tunnel, which causes a small shift in the wave front, as shown in Fig. 10. It is interesting to note that Wei et al.[4] also found a far lower value of k_2 than the value suggested by the physical spacing of the flaps. This suggests that the use of many, closely-spaced flaps does not in and of itself preclude the generation of a Sears-type gust, despite their wakes generating some spatial variation in the inflow, but that conditions in the wind tunnel must be extremely uniform to prevent any slanting of the wavefront.

In the analysis below, it will be shown that the lower value of k_2 also gives far closer agreement between the Atassi

function and experimental data. In the following analysis, the Atassi function will be evaluated at the appropriate value of k_2 for each gust amplitude.

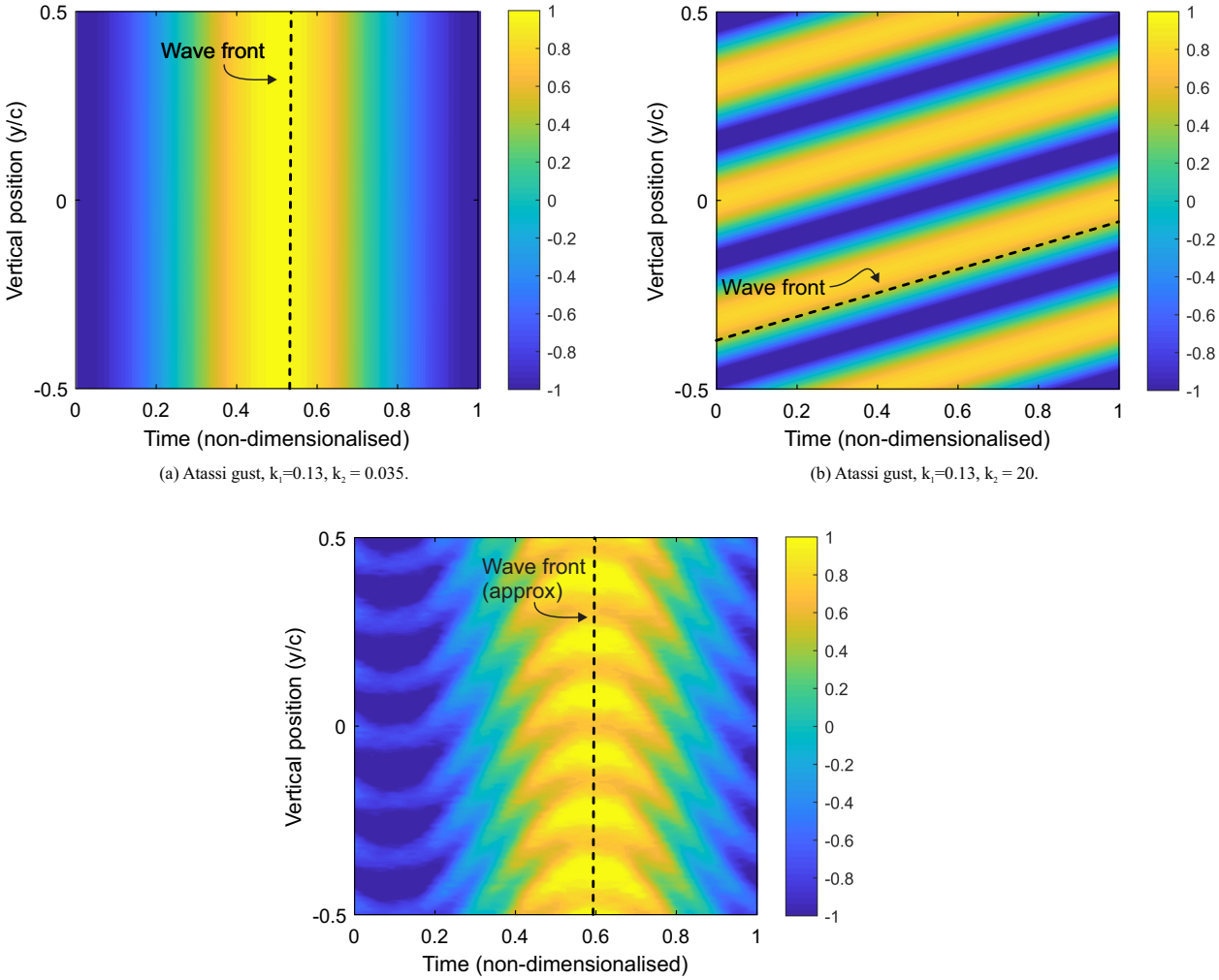

(a) Atassi gust, k_1=0.13, k_2 = 0.035.

(b) Atassi gust, k_1=0.13, k_2 = 20.

(c) Experimental data, k_1=0.13.

Fig. 10 Space-time plots of flow angle (normalised by $\hat{\alpha}_G$) for theoretical Atassi-type gusts with two different values of k_2 compared with experimental data.

C. Comparing analytical theory and experiments

Figure 11 shows the amplitude of the unsteady lift against k_1, calculated from the unsteady transfer functions and measured in experiments. Figure 11(a) shows the load amplitude normalised by the quasi-steady lift as defined by Sears (Eq. 9), while Fig. 11(b) uses the quasi-steady lift defined for the Atassi function (Eq. 10). The data is taken from tests at -0.7° mean angle of attack, which was the closest to zero of the available data range. The Atassi function is evaluated for the same aerofoil parameters, with k_2=0.035. Fig. 11(a) shows that in these conditions the Sears and Atassi functions are nearly identical when normalised consistently, and only diverge at low reduced frequencies

(k_1 <0.1).

The experimental results in Fig. 11 have been categorised by gust amplitude. The data from the two smaller gust amplitudes (blue dots $\hat{\alpha}_G = 1°$, and black dots $\hat{\alpha}_G = 2°$) agree relatively well with the transfer function, but consistently have slightly higher amplitudes. The difference is, however, within the error margin of the experiment: as stated in Section III the estimated error in the peak-to-peak gust amplitude measurements (by which the data is normalised) is ±0.25°. Representative error bars have been added to the data in Fig. 11(a). It can be seen that the uncertainty becomes larger as the gust size reduces. This shows that the normalisation of the data for comparison with the theoretical transfer functions is very sensitive to gust amplitude, and that even with relatively accurate measurements of the gust the uncertainty is large. It is important to note, however, that the error will be a constant percentage of all measurements with a given gust size.

The data from the largest gust amplitudes (red dots $\hat{\alpha}_G = 3°$) consistently shows lift amplitudes that are substantially lower than that predicted by Sears and Atassi. The reason for this is not apparent, but it may be caused by second-order non-linear effects caused by the large forcing amplitude meaning that the linear approximation implicit in analytical transfer functions is no longer valid. It could be that this largest gust amplitude (a peak-to-peak amplitude of 6°) causes viscous separation on the aerofoil. This, however, seems unlikely, as the mean angle of attack is far from the static stall angle and there was no evidence of stall in the surface pressure measurements.

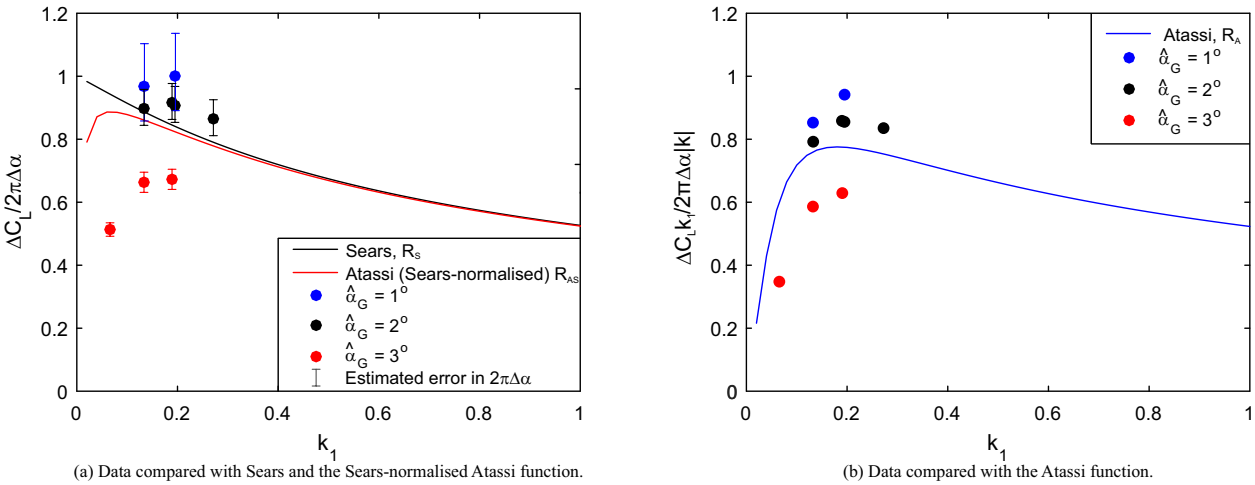

(a) Data compared with Sears and the Sears-normalised Atassi function.

(b) Data compared with the Atassi function.

Fig. 11 Comparison of experimental data with the Sears and Atassi transfer functions with the aerofoil at a mean incidence of -0.7° across a range of gust amplitudes, $\hat{\alpha}_G$, and reduced frequencies, k_1.

The mean angle of attack ($\alpha = -0.7°$) for the results in Fig. 11 was chosen such that the distorting effects of the aerofoil potential field were small, meaning that the Sears and Atassi functions gave similar results. Below, in Figs 12 and 13, the lift amplitude is shown against the changing mean angle of attack (α), in order to illustrate the effect of changing the aerofoil potential field. In these figures the lift amplitude has been normalised by the quasi-steady lift amplitude as defined by Sears (Eq. 9).

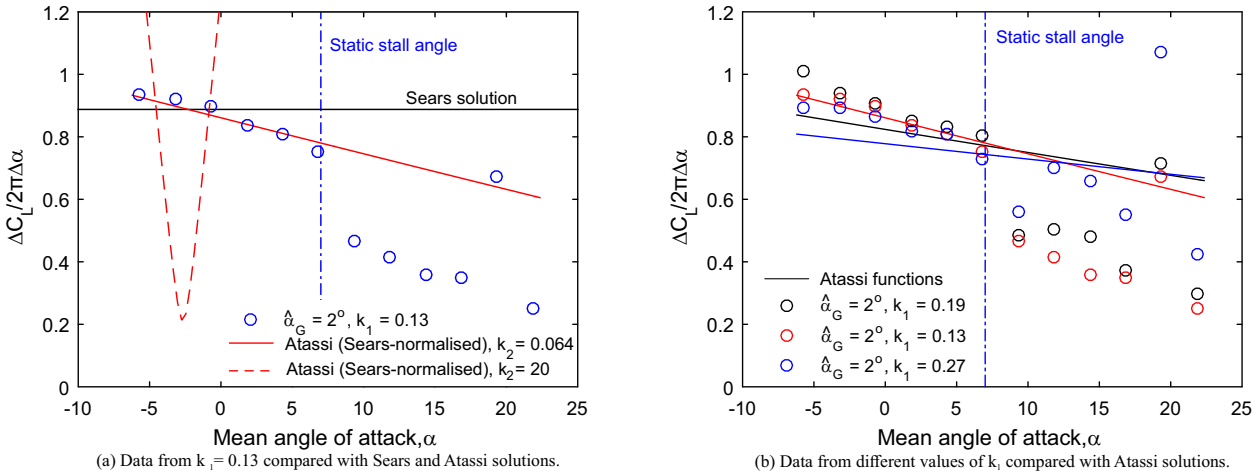

(a) Data from k_1 = 0.13 compared with Sears and Atassi solutions.

(b) Data from different values of k_1 compared with Atassi solutions.

Fig. 12 Amplitude of unsteady response against angle of attack, normalised by quasi-steady response as defined by Sears compared with the Sears and Atassi functions ($\hat{\alpha}_G = 2°$).

Figure 12 shows the results for experimental gust amplitude $\hat{\alpha}_G = 2°$. Figure 12(a) shows the results from a single experimental run (blue circles), and compares the data with both the Sears (black line) and Atassi (red line) functions. Figure 12(a) shows that there is a marked reduction in the unsteady load response as the angle of attack increases. The Sears function does not model the effect of angle of attack, and therefore the solution is constant for all α. This means that the Sears solution disagrees with the experimental data when the angle of attack is not negligible. The Sears and Atassi solutions cross near the angle at which the aerofoil produces zero lift, as this is the point at which the effect of the aerofoil potential field switches sign.

The Atassi function is evaluated at $k_2 = 0.064$ in Fig. 12(a), which was the value obtained from the 2-parameter fit for this gust amplitude (see Fig. 9). As an illustration, the Atassi function is also shown evaluated with $k_2 = 20$ (red dashed line), which was the original visual estimate of k_2 from Fig. 6(a). With the higher value of k_2, the Atassi function gives a much more dramatic variation in lift with changing α, indicating that the value of k_2 calculated from the two-parameter fit is the appropriate one to use, rather than the visual estimate.

The vertical dash-dot line in Fig. 12(a) indicates the static stall angle of the aerofoil (see Fig. 4(a)). Below this angle, the agreement between the experiment and the Atassi function is good. After this the agreement deteriorates, as is expected when the viscous effects of a stalled aerofoil impact the results. There is a peak in the unsteady response at $\alpha = 20°$. This is observed in all tests and may be a coupling of the aerofoil dyanmic stall with the jet boundaries.

Figure 12(b) shows the data in Fig. 12(a) (red circles) along with measurements from tests at two higher values of k_1. The Atassi function evaluated at the respective values of k_1 is shown as solid lines of corresponding colour. Again, the trend of reducing lift amplitude with increasing $\left(\hat{L}_{QS}\right)_S$ agrees with Atassi up to the static stall angle of the aerofoil, though there is some disagreement at lower angles of attack.

Fig. 13 shows plots of unsteady load amplitude against angle of attack, for the experiments with gust amplitudes ($\hat{\alpha}_G$)

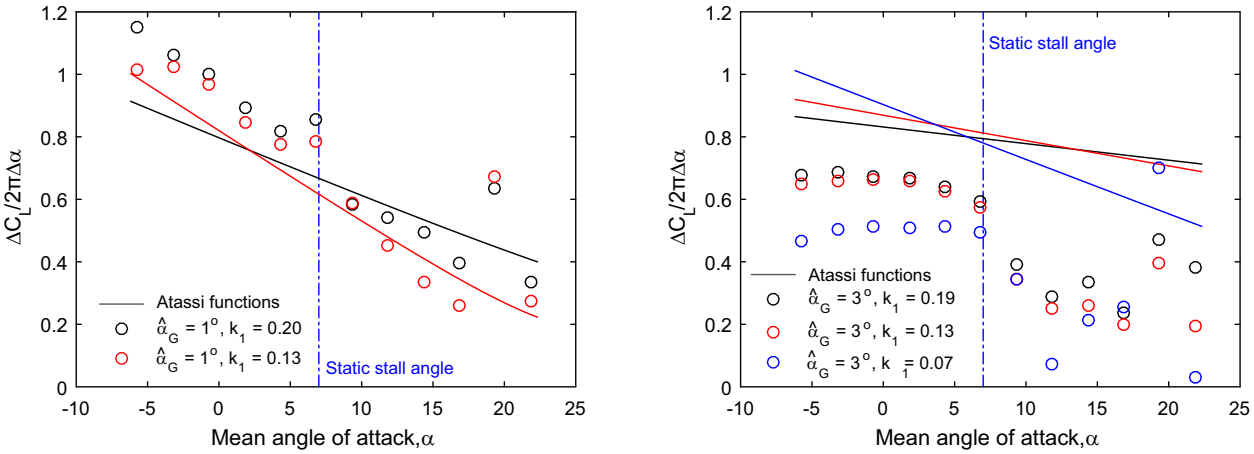

(a) Gust amplitude, $\hat{\alpha}_G$=1°. (b) Gust amplitude, $\hat{\alpha}_G$= 3°.

Fig. 13 The amplitude of the unsteady response, normalised by the quasi-steady response as defined for the Sears function, for increasing mean angle of attack, compared with the Atassi function with two different gust amplitudes.

of 1° (Fig. 13(a)) and 3° (Fig. 13(b)). In Fig. 13(a), the gradient of the unsteady lift response follows the Atassi function very well, although the magnitude of the response is slightly under-predicted by the Atassi function. Again, this difference is within the error margin for measurements of the gust amplitude, by which the response is normalised. The deterioration in agreement at angles above the static stall angle previously observed in Fig. 12 is less clear with the smaller gust amplitude, though the same peak is observed at 20° angle of attack.

Figure 13(b) shows the normalised lift against mean angle of attack for the largest gust amplitude ($\hat{\alpha}_G$ = 3°). The experimental results are consistently 50-70% of the unsteady lift amplitude predicted by Atassi, and the gradient of the unsteady lift response is not well-predicted. As discussed in relation to Fig. 11, this is likely to be due to the large-amplitude gust causing second-order non-linear effects. Beyond the static stall angle the unsteady effects are dramatic, and some very large lift amplitudes suggest the presence of dynamic stall (which is also seen in Fig 13(a), and in Fig. 12).

The results in Figs 12 and 13 suggest that the Atassi function correctly represents the coupling between the aerofoil potential field and the gust, and its effect on the unsteady lift response. Furthermore, the results emphasise the importance of correct evaluating k_2, which should be found through a 2-parameter fit using Eq. 4, as shown by Wei et al. [4].

It is also worth noting that the Atassi function does not account for thickness, even though Goldstein and Atassi suggest that the effect of thickness may be of the same order of magnitude as that of camber and incidence angle [2]. Given that the aerofoil used in this work has significant thickness (21% chord), this may account for some of the discrepancies observed.

VII. Speed of gust propagation along the aerofoil

As discussed in Section V, the potential flow upstream of the aerofoil has been shown to superpose linearly onto the gust, in line with the assertion of Goldstein and Atassi [2]. Goldstein and Atassi, however, predict that aerofoil loading *will* cause a difference in the propagation of the gust along the two surfaces, and state that this has an important effect on the unsteady response of the aerofoil. The effect of the aerofoil loading is to increase the convection speed of the vortical gust on the suction surface, where the flow velocity is higher than the freestream velocity, while decreasing the convection speed on the pressure surface, where the flow velocity is lower than the freestream velocity.

From the Fourier analysis described in Section VI, the phase of the pressure fluctuations at each point on the aerofoil surface can be calculated:

$$\phi = \tan^{-1}\left(\frac{B_N}{A_N}\right) \tag{18}$$

The phases calculated in this way are plotted against axial position for four selected cases in Fig. 14. It should be noted that the pressure moves in opposite directions on the two surfaces (i.e. an increase in incidence causes a reduction in the pressure on the suction surface and an increase on the pressure surface), so if the two surfaces were responding 'in phase' with one another there would be an offset of π radians in their calculated phase. In order to aid comparison, the suction surface data has been shifted by π radians. The data are all shown relative to the phase of the leading edge pressure transducer. The unsteady loading is mainly concentrated over the front portion of the aerfoil, and so the response magnitude is very low over the rear of the aerofoil. This means that the measurement accuracy is low at the rear of the aerofoil, and so there is a large amount of scatter in the data in this region. For this reason, phase data is only shown up to $x/c = 0.6$, though measurements were taken up to 85% of chord.

Figure 14(a) shows the phase lag of the response at two different reduced frequencies. In both cases, the gust amplitude, $\hat{\alpha}_G$, is 2° and the aerofoil incidence is 1.8°. For each case shown, a straight line fit has been applied to the data from between the leading edge and $x/c = 0.34$, and a dashed line shows the path of the gust if it were to convect at the free-stream velocity, which is given by:

$$\Delta\phi_{\text{frozen}} = 2\pi\frac{T_{\text{gust}}}{T_{\text{conv}}} = 2\pi\frac{c}{U_\infty}\frac{k_1 U_\infty}{2\pi c} = k_1 \tag{19}$$

where T_{gust} is the gust timeperiod and T_{conv} is the time taken for the freestream flow to pass over the aerofoil.

Considering first the data from $k_1 = 0.13$ (denoted by circles), it can be seen that the phase follows a different trajectory on the two surfaces. On the pressure surface (shown in blue), a small phase lag develops over the aerofoil, which is roughly equal to that of a frozen gust (dash-dot line). On the suction surface (shown in red), however, the increase in phase lag over the chord is much larger than that of a frozen gust. This is due to the stretching of the gust

on the suction surface [2].

At the higher reduced frequency (k_1 = 0.27, denoted by squares), the same trend is observed, with the pressure surface data (green) lying close to the dashed line denoting the frozen gust propagation. The suction surface data (cyan) shows a much greater phase lag, again due to the stretching of the gust. The difference between the two aerofoil surfaces appears to be larger at the higher reduced frequency, but this is not always observed. Eq. 19 suggests that the phase lag across the aerofoil should increase with reduced frequency, but the response of the aerofoil will also affect the phase, and these effects are unlikely to superpose linearly.

Figure 14(b) shows the effect of aerofoil incidence on the phase change across the surfaces. The blue and red circles denote the phase on the pressure and suction surfaces, respectively, from a test with the aerofoil at -0.7° incidence, while the cyan and green squares are from a test with the aerofoil at 6.8° incidence. In these cases, the reduced frequency was fixed at 0.13 and $\hat{\alpha}_G$ was 3°. Again, the frozen gust phase is denoted by the dash-dot line. As in the previous cases, the phase lag increases more on the suction surface than the pressure surface. In these cases, it seems that the pressure surface phase lag is increasing more slowly than the frozen gust, and perhaps not at all in the higher incidence case. A difference can also be observed between the two cases - the higher incidence case shows a larger difference in the phase lag between the two aerofoil surfaces. This change between the two incidences can be attributed to the increase in loading with increased mean incidence and the accompanying increase in flow velocity changes across the aerofoil surfaces.

This analysis shows that there is a difference between the gust propagation across the aerofoil surfaces, with the phase lag increasing more on the suction surface than the pressure surface. The differences in local flow speed cause the gust to travel faster on the suction surface and slower on the pressure surface. This finding is in line with the argument of Goldstein and Atassi [2], and suggests that their model therefore is capturing the major effect of the aerofoil potential field on the unsteady load response.

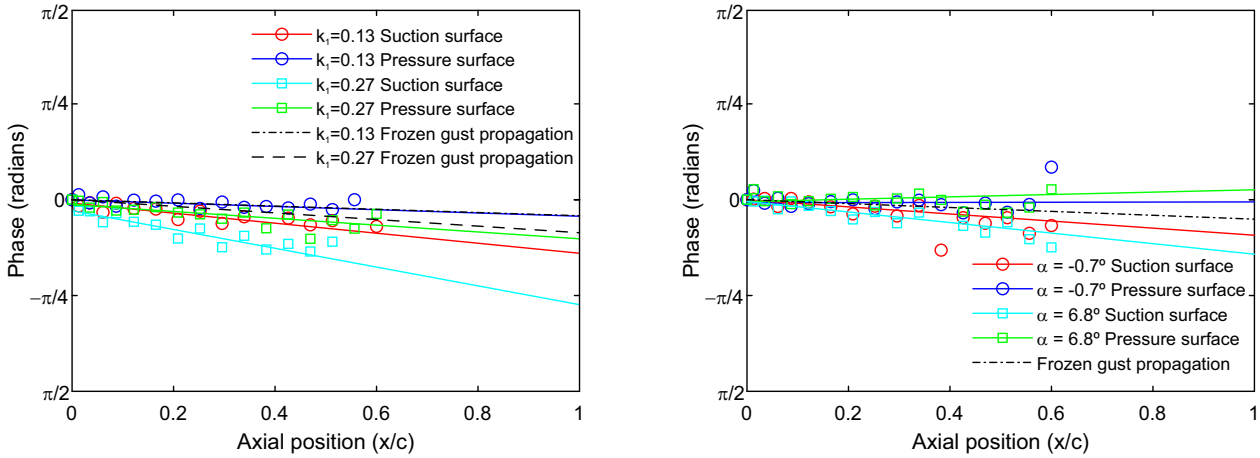

(a) Effect of reduced frequency with α= 1.8° and $\hat{\alpha}_G$ = 2°.

(b) Effect of aerofoil incidence with k_1 = 0.13 and $\hat{\alpha}_G$ = 3°.

Fig. 14 Axial variation in phase of the response calculated from aerofoil surface pressure signals.

VIII. Conclusion

This paper has presented an examination of the unsteady load generated by an Atassi-type gust on an aerofoil with non-zero mean load. The results presented above suggest that the Atassi function can predict the effect of changes in mean aerofoil loading on the unsteady lift experienced by aerofoils, for transverse gusts with a streamwise oscillating component. In cases with small-to-moderate gust amplitude, the trends in unsteady response are replicated accurately in terms of the effects of both reduced frequency and aerofoil angle of attack. The agreement is good when the mean angle of attack is smaller than the static stall angle of the aerofoil; at higher angle of attack the lift response is more erratic and the agreement deteriorates.

With very small gust amplitudes, the experimental error in measuring the gust generates substantial uncertainty in the quasi-steady response, and so the absolute magnitude of the data may not be reliable. With very large gust amplitudes, the trends in the data are also not replicated by the Atassi function, suggesting that the second-order non-linear effects have become significant.

One limitation of the Atassi function is that aerofoil thickness is not accounted for, although Goldstein and Atassi suggest that the effect of thickness may be of the same order of magnitude as that of camber and incidence angle [2]. The aerofoil used in the experiments above is chosen to represent the aerofoil section of a tidal turbine blade, which are generally thicker than those of for example wind turbines or aircraft. As such, discrepancies between the Atassi function and experiments could be caused by thickness effects.

Examination of the flowfield upstream of the aerofoil has shown that the gust and the aerofoil potential field can be considered to superpose linearly, i.e. there is no unsteady coupling of the incoming gust with the potential field. This was shown by comparing gust measurements with the aerofoil in place with the gust obtained by adding the quasi-steady potential field to the gust measured in the empty wind tunnel. This finding is in line with the analysis of Goldstein and Atassi [2].

The phase of the surface pressure measurements was used to examine the propagation of the gust along each surface of the aerofoil. Again, this data agrees with the statement of Goldstein and Atassi that the gust convection speed is increased, elongating the gust, on the suction surface, and similarly compressing the gust on the pressure surface due to the lower local convection speed.

Overall, this paper shows first-of-a-kind validation of the Atassi function for an aerofoil with non-zero mean load encountering a gust with both streamwise and transverse components. Furthermore, the results presented here suggest that gust generation through the use of many small vanes generates gusts with very low k_2 values, despite some visual images of the flow field suggesting otherwise. Because of this, the lift amplitude was a relatively weak function of the mean angle of attack and camber, compared to what it would be at higher k_2.

Funding Sources

The experiments described in this paper were funded by EPSRC grant EP/J010308/1. Dr Young was funded by the Maudslay-Butler Research Fellowship at Pembroke College, Cambridge, and by EPSRC grant EP/L015943/1. Dr Smyth was funded by an EPSRC Doctoral Training Grant at the University of Cambridge, and by an EPSRC Doctoral Fellowship.

Acknowledgements

The authors wish to thank the technical staff of the Whittle Laboratory for their assistance in manufacturing the gust generator and test section - in particular, Mr David Barlow, Mr Ian Thornton and Mr Elliot Read. The authors would also like to thank Dr Ivor Day, Prof. Robert Miller, Dr Carl Sequeira and Mr Chris Freeman for the useful discussions during the course of this work.

References

[1] von Kármán, T., "Airfoil theory for non-uniform motion," *Journal of the Aeronautical Sciences*, Vol. 5, No. 10, 1938, pp. 379–390. https://doi.org/10.2514/8.674.

[2] Goldstein, M. E., and Atassi, H., "A complete second-order theory for the unsteady flow about an airfoil due to a periodic gust," *Journal of Fluid Mechanics*, Vol. 74, No. 4, 1976, pp. 741–765. https://doi.org/10.1017/S0022112076002036.

[3] Atassi, H., "The Sears problem for a lifting airfoil revisited-new results," *Journal of Fluid Mechanics*, Vol. 141, 1984, pp. 109–122. https://doi.org/10.1017/S0022112084000768.

[4] Wei, N. J., Kissing, J., Wester, T. T., Wegt, S., Schiffmann, K., Jakirlic, S., Hölling, M., Peinke, J., and Tropea, C., "Insights into the periodic gust response of airfoils," *Journal of Fluid Mechanics*, Vol. 876, 2019, pp. 237–263. https://doi.org/10.1017/jfm.2019.537.

[5] Jancauskas, E., and Melbourne, W., "The aerodynamic admittance of two-dimensional rectangular section cylinders in smooth flow," *Journal of Wind Engineering and Industrial Aerodynamics*, Vol. 23, 1986, pp. 395 – 408. https://doi.org/https://doi.org/10.1016/0167-6105(86)90057-7, special Issue 6th Colloquium on Industrial Aerodynamics Building Aerodynamics.

[6] Holmes, D., "Lift and measurements in an aerofoil in unsteady flow," *Turbo Expo: Power for Land, Sea, and Air*, Vol. 79801, American Society of Mechanical Engineers, 1973, p. V001T01A041. https://doi.org/10.1115/73-GT-41.

[7] Sequeira, C. L., and Miller, R. J., "Unsteady gust response of tidal stream turbines," *2014 Oceans – St. John's*, 2014, pp. 1–10. https://doi.org/10.1109/OCEANS.2014.7003026.

[8] Cordes, U., Kampers, G., Meißner, T., Tropea, C., Peinke, J., and Hölling, M., "Note on the limitations of the Theodorsen and Sears functions," *Journal of Fluid Mechanics*, Vol. 811, 2017. https://doi.org/10.1017/jfm.2016.780.

[9] Traphan, D., Wester, T., Peinke, J., and Guelker, G., "On the aerodynamic behavior of an airfoil under tailored turbulent inflow conditions," *5th International Conference on Experimental Fluid Mechanics ICEFM 2018 Munich*, 2018. https://doi.org/10.18726/2018_2.

[10] Englund, D., and Richards, W. B., "The infinite line pressure probe," *NASA Technical Memorandum*, Vol. 24, 1985.

[11] Brooks, T., Marcolini, M., and Pope, D., "Airfoil trailing edge flow measurements and comparison with theory, incorporating open wind tunnel corrections," *9th Aeroacoustics Conference*, 1984, p. 2266. https://doi.org/10.2514/6.1984-2266.

[12] Brooks, T. F., Marcolini, M. A., and Pope, D. S., "Airfoil trailing-edge flow measurements," *AIAA journal*, Vol. 24, No. 8, 1986, pp. 1245–1251. https://doi.org/10.2514/3.9426.

[13] Brooks, T. F., Pope, D. S., and Marcolini, M. A., "Airfoil self-noise and prediction," *NASA Reference Publication 1218*, 1989.

[14] Drela, M., *A user's guide to MSES 3.00*, MIT, 2004.

[15] Moreau, S., Henner, M., Iaccarino, G., Wang, M., and Roger, M., "Analysis of flow conditions in freejet experiments for studying airfoil self-noise," *AIAA journal*, Vol. 41, No. 10, 2003, pp. 1895–1905. https://doi.org/10.2514/2.1905.